Tertiary lymphoid structures are associated with enhanced macrophage and dendritic cell activation and proximity to CD8+ T cells, which better predict the clinical outcome of cervical cancer patients

Laurent Gorvel[1,2,*], Marylou Panouillot[3], Marie-Sarah Rouvière[1,2], Jumaporn Sonongbua[1], Stéphane Fattori[1], Nicolas Boucherit[1,2], Amira Ben Amara[1], Olivia Quilichini[5], Samuel Granjeaud[7], Clara Degos[1], Xavier Carcopino[6], Eric Lambaudie[5], Anne-Sophie Chretien[2], Renaud Sabatier[4], Marie-Caroline Dieu-Nosjean[3] and Daniel Olive[1,2*].

Affiliations:

1: Immunity and Cancer Team, Cancer Research Center of Marseille, CRCM, INSERM U1068, CNRS UMR7258, Aix-Marseille University U105, Marseille, France

2: Immunomonitoring Platform, Cancer Research Center of Marseille, CRCM, INSERM U1068, CNRS UMR7258, Aix-Marseille University U105, Marseille, France

3: UMRS1135 Sorbonne University, INSERM U1135, Centre of Immunology and Microbial Infections (Cimi), Immune Microenvironment and Immunotherapy Team, Paris, France

4: Paoli-Calmettes Institute, Predictive Oncology Laboratory, Cancer Research Center of Marseille, CRCM, INSERM U1068, CNRS UMR7258, Aix-Marseille University U105, Marseille, France

5: Department of Surgical Oncology, Institut Paoli-Calmettes, Marseille, France

6: Department of Obstetrics and Gynecology, Hôpital Nord, APHM, Aix-Marseille University (AMU), CNRS, IRD, IMBE UMR 7263, 13397, Marseille, France

7: CRCM Integrative Bioinformatics Platform, Cancer Research Center of Marseille, CRCM, INSERM U1068, CNRS UMR7258, Aix-Marseille University U105, Marseille, France

*corresponding authors

Abstract

Cervical tumors are usually treated using surgery, chemotherapy, and radiotherapy, and would benefit from immunotherapies. However, the immune microenvironment in cervical cancer remains poorly described. Tertiary lymphoid structures (TLS) were recently described as markers for better immunotherapy response and overall better prognosis in cancer patients. We integratedly evaluated the cervical tumor immune microenvironment, and specifically TLS importance, using combined high-throughput phenotyping, soluble factor dosage, spatial interaction analyses, and statistical analyses. We demonstrate that TLS presence is associated with a more inflammatory soluble microenvironment, with the presence of B cells as well as more activated macrophages and dendritic cells (DCs). Furthermore, this myeloid cell activation is associated with expression of immune checkpoints, such as PD-L1 and CD40, and close proximity of activated conventional DC2 to $CD8^+$ T cells, therefore indicating better immune interactions and tumor control. Finally, we associate TLS presence, greater B cell density, and activated DC density to improved progression-free survival, and present it as an independent prognostic marker. To conclude, our results provide an exhaustive depiction of the cervical tumor immune microenvironment where TLS presence marks cell activation and immunotherapy target expression. These findings may provide predictive clues for patient response to targeted immunotherapies.

42 **Introduction**

43 Cervical cancer is the fourth most common cancer in women and is still a public health issue in
44 developing countries[1]. Cervical tumors are human papillomavirus (HPV)-positive in more than 95% of
45 cases. Vaccination against HPV provides good protection against the development of cervical tumors;
46 however, vaccination rates remain low worldwide (50% in both Europe and the USA)[1]. Most cervical
47 tumors comprise well-infiltrated squamous cell carcinomas (SCC), the rest being less-infiltrated
48 adenocarcinomas (ADK)[2]. Cervical SCCs are usually associated with better overall survival (OS) than ADKs
49 (5-year OS rates of 80% and 60%, respectively). Tumor severity is defined by International Federation of
50 Gynecology and Obstetrics (FIGO) stages, where a higher FIGO stage corresponds to worse severity,
51 lymph node (LN) invasion and metastasis, and correlates with poorer OS (decreasing to 55% at 5 years
52 for FIGO stage IVa)[3]. Cervical tumors are treated using surgery and brachytherapy and chemotherapy.
53 These are debilitating treatments, especially for younger women in age to expect children.
54 Immunotherapies provide an advantageous set of treatment as they often present less toxicities than
55 chemotherapy or radiations. However, they require a well described immune environment, which is
56 currently understudied in cervical tumors. It is known that the T cell compartment harbors regulatory T
57 cells (Tregs), which are often associated with poor prognosis, and tumor-infiltrating conventional $CD4^+$
58 and $CD8^+$ T cells, including HPV-specific T cells. The latter respond to HPV oncogenic protein E7 or viral
59 capsid proteins in the tumor microenvironment and usually improve patient outcome by killing HPV-
60 releasing cells[4, 5, 6]. The myeloid compartment is less well studied, with research focusing on the Tumor-
61 Associated Macrophage (TAM) infiltrate and phenotype in the tumor bed and how these associate with
62 survival. Overall, whether they express CD163, CD206, or CD204, TAMs are associated with advanced
63 FIGO stages[7, 8, 9, 10]. Interestingly, the expression of programmed death-ligand 1 (PD-L1) by TAM is
64 associated with programmed death-1 (PD-1) expression in the $CD8^+$ and $CD4^+$ T cell compartments and
65 improves prognosis when the ratio is in favor of $CD8^+$ T cell infiltrate[11, 12, 13]. However, most of these
66 studies only correlate presence or absence of specific cell types to prognosis or therapy response, and do
67 not assess their spatial distribution within the tumor microenvironment. Determining the localization
68 and interactions of subsets of immune cells in the stroma, or within the tumor nests, of a tumor type is
69 now critical to understanding tumor-specific treatment responses. Indeed, the organization of the
70 immune infiltrate, particularly into tertiary lymphoid structures (TLS) within the tumor, has been
71 associated with improved prognosis and response to immunotherapy in cancer patients[14]. TLS are
72 organized aggregates of immune cells which develop at the site of chronic inflammation and display a
73 similar organization to secondary lymphoid organs[15]. Indeed, TLS exhibit a B cell zone that includes

74 mainly germinal center B cells and follicular dendritic cells (FDCs), adjacent to a T cell zone comprising
75 mainly T cells and activated DCs (aDCs)[16, 17]. As TLS are heterogeneous, they warrant further investigation
76 in specific tumor microenvironments, as both their composition and the associated overall immune
77 infiltrate may provide insights for tumor-specific therapies and biomarkers[14]. The presence of TLS within
78 cervical tumors has not been directly demonstrated yet and remains at the gene signature detection
79 level[18]. However, TLS presence in HPV-positive head and neck SCCs (HNSCCs) is associated with a higher
80 B cell infiltrate and follicular helper T cells (Tfh)[19]. A greater proportion of myeloid cells and $CD8^+$ T cells
81 in the vicinity of the TLS has also been reported. Together, these parameters are associated with an
82 improved prognosis in patients with HPV-positive HNSCC. Among the gynecological cancers, endometrial
83 tumors are reported to harbor TLS[20], and these are associated with improved prognosis in microsatellite
84 instability (MSI) endometrial tumors, allowing stratification for immunotherapy within this patient
85 group[20]. Indeed, the improved prognosis seen in MSI patients suggests that the presence of TLS and its
86 associated immune infiltrate should be added to the molecular classification of endometrial cancer[20].

87 Given these findings in other tumor types, integrated investigation of the cervical tumor immune
88 infiltrate is clearly warranted to understand the different cellular compartments and their interactions.
89 Here, we present an in-depth study of TLS presence in the cervical cancer immune microenvironment
90 and its impact on the overall immune infiltrate, at both the cellular and spatial levels, and how these
91 parameters may contribute to overall prognosis and therapy response.

92

93 ## Results

94 **TLS in cervical tumors are associated with B cell density, dendritic cell activation, and a higher**
95 **inflammatory profile.**

96 We evaluated the presence of TLS in 34 cervical cancer samples. TLS-positive tumors represented
97 50% (17/34) of the studied specimen (**Fig. 1A**). TLS-positive (TLS^+) tumors showed an increased density of
98 aDCs and B cells, compared to TLS-negative (TLS^-) tumors, and a correlation between the two cell types
99 (**Fig. 1B, 1C, 1D**). **Fig. 1E** displays a mature TLS exhibiting a B cell zone ($CD20^+$ B cell and $CD21^+$ FDC
100 cluster) and a T cell zone ($CD3^+$ T cell and DC-$LAMP^+$ aDC cluster) and the presence of high endothelial
101 venules ($PNAd^+$ cells). Next, by measuring secreted cytokines, soluble effectors and chemokines in TLS^+
102 tumor, TLS^- tumor and healthy cervix dissociation supernatants, we determined that TLS presence is
103 associated with inflammation. IFN-α2, IL2-Rα, IL-16, TNF-α, TRAIL, CCL3, CCL4, CCL5, CXCL9 and CXCL10

104 concentration increased in TLS$^+$ tumors compared to healthy cervix, while only IL2-Rα, TRAIL, CCL3, CCL4
105 and CXCL10 increased in TLS$^-$ tumors compared to healthy cervix (**Fig. 1F**). We observed no significant
106 differences between TLS$^+$ and TLS$^-$ tumors, although CCL3, IL-16 and TNF-α tended to increase in TLS$^+$
107 samples (**Fig. 1F**). In summary, our results show that TLS is present in 50% of cervical tumors, is
108 associated with higher densities of B cells and aDC, and tends to be associated with a more inflammatory
109 profile.

110

111 **TLS$^+$ tumors exhibit a higher B cell infiltrate characterized by an enrichment of plasmablasts in the**
112 **stromal compartment and exacerbated IgG presence**

113 We analyzed the B cell, myeloid, and T cell compartments in TLS$^+$ and TLS$^-$ tumors by flow
114 cytometry. First, we investigated the B cell compartment by flow cytometry and unsupervised analysis.
115 We mapped B cells using h-SNE (hierarchical stochastic neighborhood embedding) and assessed the
116 clustering by cell density. In total, we identified 8 B cell clusters and annotated them according to the
117 differential expression of CD5, IgD, CD27, CD24, CD38, and CD21 (**Fig. 2A**). The absolute number of B
118 cells was higher in TLS$^+$ tumors as compared to TLS$^-$ tumors (**Fig. 2B**). The density clustering defined
119 CD5$^+$IgD$^+$ B cells, CD5$^+$CD69$^+$IgD$^-$ B cells, naïve B cells (CD27$^-$IgD$^+$), CD69$^-$ resting memory (RM) B cells,
120 CD69$^+$ activated memory (AM) B cells, tissue-like memory B cells (TLM, CD21$^-$CD27$^-$), germinal center B
121 cells (GC, CD38^{lo}IgD$^-$), and plasmablasts (IgD$^-$CD86$^+$CD38^{hi}). None of these subset frequencies were
122 significantly different in TLS$^+$ vs. TLS$^-$ tumors (**Fig. 2C**). As subsets did not seem to vary, we investigated
123 the spatial localization of B cells within the cervical tumor and stroma by multiplex immunofluorescence
124 (IF) as shown in **Fig. 2D**. Briefly, we applied the tumor nest region of interest (ROI), determined as pan-
125 cytokeratin positive (PanCk$^+$), to all samples (6 TLS$^+$ and 6 TLS$^-$). The absence of PanCk staining identified
126 the stroma ROI. We observed no significant differences in CD20$^+$CD138$^-$ B cells, CD20$^+$CD138$^+$
127 plasmablasts, and CD20$^-$CD138$^+$ plasma cells between TLS$^-$ and TLS$^+$ samples in the tumor nest (**Fig. 2E**).
128 Plasmablasts infiltrated TLS$^+$ stroma significantly more than TLS$^-$ stroma (**Fig. 2F**). Notably, CD20$^-$ plasma
129 cells and B cells did not vary between TLS$^+$ and TLS$^-$ stroma (**Fig. 2F**). Considering the increase in
130 plasmablasts in TLS$^+$ stroma, we assessed the presence of soluble immunoglobulins (Ig) in TLS$^+$, TLS$^-$ and
131 healthy cervix supernatants, and found significant increases in IgG1, IgG2, IgG3, IgA, IgM, IgD and IgE in
132 TLS$^+$ sample supernatants compared to those of healthy cervix (**Fig. 2G**). However, TLS$^-$ sample
133 supernatants were also enriched in IgG3, IgD, IgA and IgM compared to healthy cervix samples. We
134 observed no statistically significant differences between the TLS$^-$ and TLS$^+$ samples, although there were

135 trends for increased IgG1, IgG2 and IgG3 levels in TLS$^+$ supernatants (**Fig. 2G**). Altogether, these results
136 suggest enrichment of the B cell compartment in TLS$^+$ tumors, in terms of the infiltrating cell number and
137 a greater diversity of Igs secreted.

138

139 **CD163$^+$ macrophages and activated cDC2 are enriched in TLS$^+$ cervical tumors**

140 The myeloid compartment is known to regulate TLS formation (macrophages)[21, 22] and to
141 participate in their T cell-activation function (aDCs)[23]. Therefore, we characterized the myeloid
142 compartment by mass cytometry and used hSNE and a density cluster analysis to map myeloid cell
143 subsets. We identified 8 clusters composed of Langerhans cells (LCs, CD1a$^+$CD11c$^+$), CD1a^{lo} DCs
144 (CD1c$^+$CD1a^{lo}), cDC1 (HLA-DR$^+$CD11c$^+$CD11b$^-$CD141$^+$), cDC2 (CD11c$^+$CD1c$^+$), pDCs (CD123$^+$CD303$^+$), early
145 myeloid-derived suppressor cells (eMDSCs, HLA-DR$^-$/^{lo}CD11b$^+$CD14$^-$CD15$^-$), monocytic MDSCs (mMDSCs,
146 HLA-DR$^{-/lo}$CD11b$^+$CD14$^+$) and TAMs (CD64$^+$CD68$^+$HLA-DR$^+$) (**Suppl. Fig. 1A, 1B**). We also divided TAMs
147 according to CD163 expression (**Fig. 3A; Suppl. Fig. 1A**). TAM numbers did not vary significantly between
148 TLS$^-$ and TLS$^+$ tumors. However, the frequency of CD163$^+$ TAMs was higher in TLS$^+$ tumors compared to
149 TLS$^-$ tumors (**Fig. 3B**). Localization of TAMs by multiplex IF showed a trend for increased CD163$^+$ TAM
150 infiltrate in TLS$^+$ sample stroma and tumor (**Fig. 3C**). Next, we assessed the infiltration of TLS$^+$ and TLS$^-$
151 samples by cDC2, LCs and CD1a^{lo} DCs, and observed an increased number of cDC2 in TLS$^+$ samples
152 compared to TLS$^-$ samples (**Fig. 3D**). Therefore, we investigated cDC2 localization using the DC-LAMP
153 marker for aDCs and CD1a for LCs. We found no difference in aDCs (CD1a$^-$DC-LAMP$^+$), activated LCs
154 (aLCs, DC-LAMP$^+$CD1a$^+$), and immature LCs (iLCs, DC-LAMP$^-$CD1a$^+$) infiltrate in the tumor ROI (PanCk$^+$).
155 However, aDCs infiltrate was significantly higher in TLS$^+$ sample stroma compared to TLS$^-$ stroma.
156 Notably, iLCs and aLCs tended to increase in TLS$^+$ stroma (**Fig. 3E**). In summary, our results show an
157 increase in differentiated macrophages and aDCs in the stroma of TLS$^+$ samples.

158

159 **Myeloid cells are more activated and better differentiated in TLS$^+$ tumors**

160 We investigated the phenotypic variations within the myeloid cell subsets. We assessed the
161 expression of PD-L1, CD40, LILRB2, CD1d, CCR2, CCR5, CXCR4, CD80, CD86, HLA-DR, PVR, Nectin2, IL-6,
162 CD10, CD206, CD209 and CD141 among LCs, CD1a^{lo}DCs, cDC1, cDC2, pDCs, eMDSCs, mMDSCs, CD163$^-$
163 TAMs, and CD163$^+$ TAMs. The obtained frequencies were filtered on a 10% average expression and a
164 minimum of 30 cells per cluster. We analyzed the resulting 101 variables (44 TLS$^+$, 57 TLS$^-$) using a

165 between-group analysis (BGA) to obtain each variable contribution to either a TLS$^+$ or TLS$^-$ profile (**Fig.**
166 **4A**). The segregation plot in **Fig. 4B** (left) shows a clear separation between TLS$^+$ and TLS$^-$ tumor states
167 with no overlap between samples for each group, suggesting that myeloid cells are a critical component
168 of TLS$^+$ tumors. CD163$^+$ TAMs were the most highly represented cell type in the TLS$^+$ group top 10
169 variables (45% of the contribution to the TLS$^+$ group), with six of the top 10 variables corresponding to
170 the contribution of CD1d, CXCR4, PD-L1, CCR2, CCR5, and CD40 expression (**Fig. 4B**; **Supplementary**
171 **Table S6**). The expression frequency of these six markers on CD163$^+$ TAMs confirmed the BGA results,
172 except for CD40 which only trended towards an increase in TLS$^+$ tumors (**Fig. 4C**). cDC2 also contributed
173 to the TLS$^+$ environment with the expression of CD40, confirmed by measuring its expression frequency
174 on cDC2 (**Fig. 4B, 4C**). Early MDSCs contributed to the TLS$^+$ group with the expression of PD-L1, CD40 and
175 CCR5 (**Fig. 4B**). However, none of these marker frequencies significantly differed from those seen in the
176 TLS$^-$ group (**Fig. 4C)**. Overall, the myeloid cell contribution to a TLS$^+$ environment is determined by the
177 expression of activation (CD40) and inhibition (PD-L1) markers, which reflects a better differentiation of
178 TAMs and cDCs. Furthermore, the contribution of chemokine receptor expression (CXCR4, CCR2, CCR5)
179 by TAMs also indicates an increase in the recruitment of these cells. The top 10 contributors to the TLS$^-$
180 group (70% of contribution) were LCs, mMDSCs, pDCs, eMDSCs, CD1a^{lo}DCs, CD163$^+$ TAMs and cDC2 (**Fig.**
181 **4B**). Here, we found intracellular IL-6 expression in cDC2 and mMDSCs, indicating a non-cytotoxic
182 inflammation. The expression of CD80 on cDC2 and CD1a^{lo} DCs contributed to the TLS$^-$ group (**Fig. 4B**).
183 Overall, our results show the importance of the myeloid cell contribution to a TLS$^+$ environment, which
184 reflects a greater differentiation and activation of mainly macrophages, and DCs.

185

186 **Spatial analysis reveals increased interactions between aDCs and CD8$^+$ T cells, which exhibit higher**
187 **diversity in TLS$^+$ tumors**

188 We hypothesized that the involvement of aDCs in the TLS$^+$ tumor characteristics was associated with
189 their proximity to CD8$^+$ T cells, and could contribute to a better immune response. Therefore, we
190 performed a proximity analysis by staining pathology slides for DC-LAMP (aDCs), CD3 and CD8 (CD8$^+$ T
191 cells) and CD1a (LCs) (**Fig. 5A**). Briefly, we performed cell segmentation and identified aDCs (DC-
192 LAMP$^+$CD1a$^-$), activated CD1a$^+$ DCs (aCD1a$^+$ DC, DC-LAMP$^+$CD1a$^+$), and CD8$^+$ T cells. Next, we quantified
193 the number of CD8$^+$ T cells within a 10 µm, 10–20 µm and 20–30 µm range of either a single aDC or
194 aCD1a$^+$ DC (**Fig. 5B**). The number of CD8$^+$ T cells within a 10 µm range of an aCD1a$^+$ DC tended to
195 increase in TLS$^+$ compared to TLS$^-$ tumors, although the difference was not significant. We observed

196 similar results within a 10–20 µm and a 20–30 µm range (**Fig. 5C**). However, the number of $CD8^+$ T cells
197 within a 10 µm range of an aDC significantly increased in TLS^+ tumors compared to TLS^- tumors (**Fig. 5D**
198 **left**), and decreased in the 10–20 µm and 20–30 µm ranges. This close proximity suggests that aDCs
199 directly interact with $CD8^+$ T cells more efficiently in TLS^+ tumors, which may contribute to improved
200 tumor control (**Fig. 5D**).

201 To further dissect the T cell response between TLS^+ and TLS^- tumors, we mapped T cell subsets by
202 CyTOF. We showed that absolute numbers of naïve ($CCR7^+CD45RA^+$), central-memory (CM,
203 $CCR7^+CD45RA$) and effector-memory $CD8^+$ T cells (EM, $CCR7^-CD45RA^-$) were increased in TLS^+ tumors,
204 which was not the case for effector-memory re-expressing CD45RA (TEMRA, $CCR7^-CD45RA^+$) $CD8^+$ T cells
205 (**Fig. 5E**). The absolute numbers of $CD4^+$ T cell subsets also varied between TLS^+ and TLS^- tumors. Indeed,
206 naïve and TEMRA $CD4^+$ T cell numbers were increased in TLS^+ tumors (**Fig. 5F**). Therefore, these results
207 show a greater diversity and differentiation of the T cells and T cell response in TLS^+ tumors.

208 Using h-SNE clustering and density clustering, we identified variations due to specific marker
209 expression by annotating each density cluster according to marker expression (heatmaps) and
210 quantifying the cluster frequencies (**Fig. 5G, 5H**). Among $CD4^+$ T cells, only EM $CD4^+$ T cells varied. Indeed,
211 EM $CD4^+$ T cells which did not express any specific checkpoint marker (**Fig. 5G** "Markerless") and
212 $CD69^+CD127^+$ EM $CD4^+$ T cells were enriched in TLS- tumors compared to TLS^+ tumors (**Fig. 5G**). Among
213 $CD8^+$ T cells, one EM specific cluster was enriched in TLS^+ tumors and was marked by the expression of
214 CD69 and PD-1 and the absence of CD28 (EM $CD69^+CD28^-PD\text{-}1^+$ $CD8^+$ T cells) (**Fig, 5H**). In summary, these
215 results show increased aDC/T cell crosstalk as well as T cell activation and immune checkpoint expression
216 in TLS^+ tumors compared to TLS^- tumors.

217

218 **TLS with higher B cell and aDC densities improve prognosis in cervical tumors**

219 We hypothesized that the enhanced activation of immune cells within TLS^+ tumors could allow
220 patient segregation and predict progression-free survival (PFS). Therefore, we performed a Pages-
221 multiple factor analysis (MFA), which allows patient segregation by quantitative parameters (DC count, B
222 cell count, age, tumor size) and qualitative parameters (FIGO stage, LN status, emboli presence, DC and B
223 cell density, TLS density), and assesses the impact of these parameters on patient survival (**Suppl. Fig.**
224 **2A**). The MFA represents these factors on a PCA (principal component analysis) and quantifies the
225 involvement on the two axes (Dim1 and Dim2) of the PCA (**Suppl. Fig, 2B**). We identified that patients are

226 well-segregated by the presence of TLS on Dim1. This segregation is enhanced by the DC and B cell
227 density parameters, allowing subdivision of patients into three groups: TLS^-, TLS^+B-DC $density^{lo}$, and
228 TLS^+B-DC $density^{hi}$ (**Fig. 6A**). Notably, LN invasion also segregated patients but according to Dim2 (**Suppl.**
229 **Fig. 2C**). B cell and DC count also increased according to Dim 1, and corresponded to increases in B cell
230 and DC densities (**Suppl. Fig. 2C**). Qualitative parameters such as FIGO stage did not allow patient
231 segregation (**Suppl. Fig. 2C**). Next, we studied patient PFS according to TLS, TLS^+B-DC $density^{lo}$ and TLS^+B-
232 DC $density^{hi}$, and found that the TLS^+B-DC $density^{hi}$ group (n=10 patients) did not include any patients
233 with death or relapse, while the TLS^+B-DC $density^{lo}$ group (n=6 patients) included one death and one
234 relapse, and the TLS^- group (n=16 patients) included one death and four relapses (**Fig. 6B**). **Fig. 6C**
235 (Kaplan-Meier curve) shows better PFS in the TLS^+B-DC $density^{hi}$ group, and similar PFS curves in the
236 TLS^+B-DC $density^{lo}$ and TLS^- groups. To validate these results, we performed an immune cell enrichment
237 analysis on the cancer genome atlas CESC dataset (TCGA) using the CIBERSORT algorithm, followed by a
238 survival analysis according to B cell, $CD8^+$ T cell, activated DC (aDCs), and $CD4^+$ TEM enrichment. B cell
239 and $CD8^+$ T cell enrichment significantly improved patient survival, while aDCs only showed a non-
240 significant trend for improved survival and $CD4^+$ TEM enrichment did not influence survival outcome
241 (**Suppl. Fig. 2D**). Finally, we scored the enrichment for TLS presence, where TLS^+ tumors are enriched for
242 B cells, aDCs and $CD8^+$ T cells. We found that TLS^+ tumors are associated with better survival compared
243 to TLS^- tumors, which validates the results from our cohort (**Fig. 6D**). In summary, TLS are associated with
244 improved PFS in cervical cancer, which correlates with B cell and aDC density.

245

246 **Discussion**

247 Our study demonstrates that TLS are associated with an overall more inflammatory profile and
248 immune infiltrate in cervical tumors. We showed that the presence of TLS is associated with better
249 differentiation and activation of macrophages and DCs, which is linked to a better $CD8^+$ T cell
250 recruitment and activation. Altogether, these parameters contribute to a better prognosis in patients
251 with TLS^+ cervical tumors.

252 We used an integrated approach to investigate TLS and the immune infiltrate in cervical tumors.
253 First, we determined an increased cytokine and chemokine signature composed of IL-16, TNF-α, IFN-α,
254 CCL5, CXCL9 and CXCL10, which has already been associated with TLS in multiple tumor models. Indeed,
255 these cytokines and chemokines were first linked to TLS in a transcriptomic signature[24] in lung cancer,

256 and were associated with better prognosis. These signatures, while marking TLS presence, also mark a
257 diverse immune cell infiltrate. TNF-α and IL-16 participate in maintaining local chronic inflammation. IL-
258 16 is described as the ligand of CD4 and as a chemoattractant for $CD4^+$ T cells, but also macrophages and
259 DC subsets[25, 26]. CXCL9 and CXCL10 are produced in response to IFN-γ presence in the tissue
260 microenvironment, and participate to T cell recruitment to HPV protein $E7^+$ hyperplastic epidermis via
261 CXCR3[27]. It has been reported that the CXCL9-10/CXCR3 axis participates in prognosis improvement in
262 estrogen receptor-negative (ER^-) breast tumors[28], but promotes progression in tongue cancer[29]. CCL5
263 allows T cell, immature DC and monocyte/macrophage recruitment[30, 31], which contributes to the
264 diversity of the immune cell infiltrate and therefore the presence of TLS. However, CCL5 was also shown
265 to participate in angiogenesis and tumor growth[32], through the recruitment of macrophages[33] and
266 cancer-associated fibroblasts, which could be prevented by neutralizing the chemokine[34] or its signaling
267 pathway[32].

268 Consequently, a TLS^+ microenvironment is associated with enriched immune cell proportions,
269 which is common among cervical cancer and other HPV^+ [19] and HPV^- tumors[15, 17, 35, 36]. As expected, the
270 analysis of the B cell compartment showed an enrichment in overall B cells within TLS^+ samples. More
271 specifically, we found an increase in $CD138^+$ plasma cells within the stromal compartment of these
272 samples. Plasma cells were associated with cytokine production, chemotaxis and carcinogenesis in a
273 single cell RNA seq study of HSILs and cervical tumors[37]. In our study, plasma cell enrichment was
274 associated with an increased abundance of intra-tumoral IgGs in TLS^+ samples. To our knowledge, no
275 previous studies exist on the intra-tumoral IgG presence in cervical tumors and its association with
276 prognosis. In cervical cancer, neutralizing IgGs directed against HPV are a good marker for the efficacy of
277 vaccination, as they prevent the formation of HPV-induced low and high grade squamous intraepithelial
278 lesions (LSILs and HSILs) and tumors[38]. However, the spontaneous clearance of HPV natural infection
279 does not necessary lead to a strong antibody-mediated protection compared to vaccination. Indeed,
280 after natural HPV clearance, IgG will only be directed against a specific HPV strain and with lower titers,
281 compared to after vaccination where IgGs are directed against more HPV strains and are more
282 abundant[39, 40]. Still, this antibody response allows protection against a secondary infection with the same
283 HPV strain, if neutralizing antibody titers are high enough[39, 40]. Therefore, the increased presence of
284 intra-tumoral IgGs in TLS^+ tumors could be linked to a better response to HPV and/or tumor antigens,
285 which would contribute to improved prognosis in TLS^+ patients.

286 Myeloid cells contribute to the regulation of immune responses in tumors[41, 42, 43, 44, 45]. aDC
287 infiltration is usually associated with a better T cell activation and overall better control of tumor
288 progression[46, 47]. In our study, we show an enrichment of $CCR2^+CD40^+$aDCs in TLS^+ samples compared to
289 TLS^- samples within cervical tumor and stroma. Here, CCR2 indicates the blood origin of aDCs and
290 increased recruitment to the tumor microenvironment. In TLS^+ samples, aDCs seem to accumulate in the
291 stroma where they interact closely with $CD8^+$ T cells. Similarly, Ruffin *et al.* demonstrated that cell-cell
292 neighborhoods are composed of myeloid cells, $CD8^+$ T cells, B cells, and conventional T cells in HNSCC
293 tumors that exhibited mature GC^+TLS and had improved prognosis[19]. In ovarian tumors, the presence of
294 antigen presenting cell niches where $CD11c^+$ myeloid cells interact with $CD8^+$ T cells potentiates anti-
295 CD28 therapy and improves prognosis[48]. By analyzing the $CD8^+$ and $CD4^+$ T cell phenotype using mass
296 cytometry we observed a more diverse infiltrate. EM, TEMRA, naïve, CM $CD4^+$, and $CD8^+$ T cells were all
297 enriched in TLS^+ tumors, while remaining at low levels in TLS^- tumors. TAMs are often associated with a
298 negative outcome. Indeed, $CD204^+$, $CD206^+$ and $CD163^+$ TAMs are associated with decreased prognosis in
299 cervical cancer[41] and many other tumor types[49, 50, 51, 52]. Here, we report an increase in the expression of
300 immune checkpoints and ligands (PD-L1, CD40) and chemokine receptors (CCR2 and CCR5) in TLS^+
301 tumors. CCR2 and CCR5 expression indicates the blood monocyte origin of TAMs in TLS^+ tumors and that
302 they are continuously being recruited. TLS are known to improve response to immunotherapies[53, 54]
303 which fits with an increased expression of immunotherapy targets, such as CD40, PD-L1, CCR2 and CCR5,
304 on TAMs and aDCs. This has been clearly established for immune checkpoint inhibitors such as anti-PD-1,
305 anti-PD-L1, and anti-CTLA-4[53, 54]. Moreover, agonistic anti-CD40 mAbs allow DCs to improve anti-tumoral
306 responses[55, 56, 57, 58]. Given our observation of increased expression of CCR2 and CCR5 on TAMs from TLS^+
307 cervical tumors, targeting these chemokine receptors might represent a new therapeutic strategy to
308 limit immunosuppressive macrophage infiltration. Indeed, CCR2/CCR5 inhibitors are currently being
309 investigated in colorectal and pancreatic cancers[59]. In addition, the CCR5 inhibitor maraviroc improved
310 the immune response in HNSCC and chordoma[33, 60], while a CCR2 inhibitor in combination with
311 bevacizumab reduced tumor size in mouse models of ovarian cancer by inhibiting the MAPK pathway[61].
312 Taken together, the increased expression of immunotherapy targets on myeloid APCs may offer more
313 therapeutic options, and their proximity to a greater $CD8^+$ T cell diversity may potentiate the response to
314 immunotherapies in TLS^+ tumors.

315 The presence of TLS segregated patients into two very distinct groups. Indeed, TLS^+ tumors
316 segregated patients according to immune variables, independently of FIGO stage, presence of emboli,
317 and LN invasion. Furthermore, TLS^+ and TLS^- tumor groups could be subdivided according to B cell and

318 aDC densities. This highlights the immune infiltration organization as a critical marker of patient
319 outcome. Indeed, we demonstrated that B cell and aDC density, which increase with TLS maturity[15],
320 refines patient segregation. TLS^+ tumors with high B cell and aDC densities were associated with
321 improved PFS, compared to TLS^+ tumors with lower B cell and aDC densities and TLS^- tumors. These
322 results are in accordance with previous studies showing that TLS maturation is associated with better
323 prognosis[15, 35, 62] and often helps stratify patients when used as an independent prognostic marker[20],
324 therapy response marker[53, 54], or for refining existing patient stratification approaches. Indeed, TLS
325 presence has refined the molecular classification of patients with endometrial tumors, by sub-stratifying
326 those with MSI into an MSI^+TLS^+ patient group with improved prognosis[20]. The improved patient
327 prognosis driven by TLS presence seems to be mainly due to a much higher infiltrate of B cells, and its
328 organization around aDCs in connection with $CD8^+$ T cells. Indeed, in HNSCC, melanoma and sarcoma, B
329 cell-alone mediated survival rates are similar to those seen in tumors with TLS presence[19, 53, 54].

330 In conclusion, our results show that TLS in cervical cancer arise from a microenvironment which
331 is more inflammatory and prone to anti-tumoral response. Indeed, we show TLS^+ tumors are enriched in
332 B cells, aDCs, macrophages and T cells. Furthermore, aDCs and macrophages are better activated and in
333 close proximity of $CD8^+$ T cells, which indicates increased myeloid activation as well as a greater potential
334 for T cell stimulation. Altogether, our results provide a comprehensive characterization of the immune
335 microenvironment in cervical tumors, in terms of phenotype, spatial organization, and immune cell
336 interactions. Furthermore, our results highlight that TLS are associated with well-differentiated cells
337 expressing immunotherapy targets, raising the possibility of TLS as a predictive marker for patient
338 response to specific therapies.

339

340 **Methods**

341 **Human tumor samples**

342 Human cervical tumor samples were obtained from patients, who were included in the
343 prospective XAC-03 (NCT02875990) and GC-Bio-IPC (NCT01977274) clinical trials, conducted from 2013
344 to 2020. The XAC-30 and GC-Bio_IPC trials were approved by the institutional review board (Comité
345 d'Orientation Stratégique (COS), Marseille, France) of the Paoli-Calmettes Institute and the Assistance
346 Publique des Hopitaux de Marseille (AP-HM), respectively. In accordance with the Declaration of
347 Helsinki, written informed consent was obtained from all patients.

348 Tumor samples were acquired prior to patients receiving any treatment. Healthy cervixes were
349 obtained from hysterectomies performed in cases of benign uterine pathologies (endometriosis and
350 fibroids). Before sampling and fixation, the cervix was assessed by a pathologist to confirm it was normal.
351 Clinical characteristics of the patients from whom samples were obtained are shown in **Table 1**.

352

353 **Immunohistochemistry staining of FFPE slides**

354 All reagents and antibodies used for multiplex immunohistochemistry assay are listed in **Suppl.**
355 **Table S1–3**. After deparaffinization of two slides for each patient, epitope retrieval was performed with
356 the Dako Target retrieval solution (Dako) at pH 6.0 in a water bath for 30 minutes (min) at 97°C. After
357 washing with TBS (Euromedex), tissue sections were treated with 3% H_20_2 at room temperature (RT) for
358 15 min to inactivate endogenous peroxidase. After washing, sections were incubated with Protein Block
359 solution for 30 min at RT. To visualize TLS, tissue sections were incubated with anti-DC-Lamp and anti-
360 CD3 antibodies for one slide, and with anti-CD20 and anti-CD21 antibodies for a second slide. After
361 washing with TBS-0.04% Tween 20, the first slide was incubated with donkey $F(ab)'_2$ anti-rat IgG-biotin
362 and donkey $F(ab)'_2$ anti-rabbit IgG-alkaline phosphatase (AP), and the second slide with goat IgG anti-
363 mouse IgG2a-biotin and goat IgG anti-mouse IgG1-AP, for 30 min at RT. After washing steps, biotin-
364 conjugated antibodies were revealed with a streptavidin-horseradish peroxidase (HRP) solution,
365 incubated for 30 min at RT. CD3 and CD21 immunostaining revelations were performed by adding SAP
366 solution; DC-LAMP and CD20 were revealed with AEC solution. Slides were coverslipped with Glycergel
367 and scanned using a Nanozoomer scanner (Hamamatsu).

368

369 **Immunofluorescence staining of FFPE slides**

370 All reagents and antibodies used for multiplex IF assay are listed in **Supplementary Tables S1–3**.
371 Epitope retrieval was performed with the Target Retrieval solution at pH 6.0 or pH 9.0, depending on the
372 primary antibody tested. Slides were incubated in a water bath for 30 min at 97°C. After washing with
373 TBS, tissue sections were treated with 3% H_20_2 at RT for 30 min, washed again and incubated with
374 Protein Block solution for 30 min at RT. To visualize TLS, tissue sections were then incubated with anti-
375 DC-LAMP antibody for 1 hour at RT. After washing with TBS-0.04% Tween 20, tissue sections were
376 incubated with goat IgG anti-rat IgG1-HRP for 30 min at RT. After washing the tissue sections with TBS-
377 0.04% Tween-20, a tyramide conjugated to AF594 was added as an amplification system and incubated

378 for 10 min at RT. After washing, the tissue sections were incubated with the Target Retrieval solution for
379 10 min at 97°C. This step allowed removal of the bound primary and secondary antibodies while
380 protecting AF594 labeling of the DC-LAMP$^+$ cells. It also enabled subsequent labeling of the same tissue
381 sections with another antibody. The procedure was repeated several times to label the same tissue
382 sections with various antibodies using tyramide conjugated to different fluorochromes. The other
383 antibodies were tested after DC-LAMP labeling in the following order: anti-CD3 revealed with F(ab)'$_2$
384 donkey anti-rabbit IgG-HRP and tyramide-CF514; anti-PanCk revealed with goat anti-mouse IgG1-HRP
385 and tyramide-AF488; anti-CD21 revealed with goat anti-mouse IgG1-HRP and tyramide-AF555; anti-CD20
386 revealed with goat anti-mouse IgG2a-BV480; and anti-PNAd revealed with F(ab)'$_2$ goat anti-rat IgGM-
387 AF647.

388 To study the B cell, CD8$^+$ T cell, and myeloid compartments, three other IF panels were performed
389 using the same techniques and various antibody combinations: anti-CD1a revealed with goat IgG anti-
390 mouse IgG1-HRP and tyramide-CF514; anti-CD8 revealed with goat IgG anti-mouse IgG1-HRP, tyramide-
391 biotine and streptavidine conjugated to AF647; anti-CD68 revealed with goat IgG anti-mouse IgG1-HRP
392 and tyramide-CF430; anti-CD138 revealed with goat anti-mouse IgG1-HRP and tyramide-CF430; anti-
393 CD163 revealed with goat anti-mouse IgG1-HRP and tyramide-AF594.

394 Nuclei were then stained with DAPI for 5 min at RT before coverslips were mounted onto the glass
395 slides with Fluorescent Mounting Medium. Slide imaging was performed using a Zeiss Axio Observer Z1
396 at 385 nm, 430 nm, 475 nm, 511 nm, 555 nm, 590 nm and 630 nm with the corresponding filters and Zen
397 software (Zeiss).

398

399 **Spatial analysis of cervical tumor FFPE sections**

400 TLS quantification and density analysis were performed using HALO® software (Indica Labs). ROI
401 were delineated, and Hematies, Blank and Necrosis regions were excluded. A classifier was used to
402 discriminate TLS, tumor nest and stroma via staining of PanCk, CD20 and CD3. A Nuclei Seg Artificial
403 Intelligence algorithm allowed identification of cells based on their nuclei staining by DAPI. A Multiplex
404 IHC v3.2 analyzer was used to count CD20$^+$ and DC-LAMP$^+$ cells in immunohistochemistry slides. A
405 HighPlex FL v4.2 analyzer was used to count cells in IF slides. Spatial analyses with proximity analysis
406 setup were used to measure the distance between immune cell types.

407

408 **Tumor sample dissociation**

409 Tumor and healthy cervix samples were processed within 4 hours following surgery. Samples were
410 minced and then dissociated using a gentleMACS dissociator (Miltenyi Biotech) in RPMI 1640 culture
411 medium. Fragments were centrifuged and supernatants were frozen for soluble factor dosage.
412 Fragments were then suspended in Gentle Dissociation Solution (StemCell) and incubated for 20 min at
413 37°C and 5% $C0_2$. Samples were again dissociated using the gentleMACS dissociator before centrifugation
414 and filtering through a 100 µm strainer. Finally, cells were counted and frozen in heat-inactivated fetal
415 calf serum 10% DMSO until staining.

416

417 **Soluble factor dosage**

418 *Chemokines, cytokines, and growth factors*

419 Supernatants were thawed at RT and used for growth factor, cytokines, and chemokines dosage by
420 Luminex using the 48-Plex pan-human cytokine kit (BioRad) according to the manufacturer procedure.
421 Briefly, supernatants were incubated with analyte-specific antibody-coated microbeads for 1–2 hours.
422 Supernatants were then washed and incubated with a PE labeled secondary antibody for MFI detection.
423 Data were acquired on a BioPlex-200 system (BioRad) and analyzed on BioPlex Manager 6.0 (BioRad),
424 comparing against standard curves for each analyte and according to manufacturer instructions. Raw
425 data were normalized against tumor sample weights.

426 *Immunoglobulins*

427 Supernatants were thawed at RT and used for IgG1-2-3-4, IgA, IgE, IgM and IgD dosage by
428 LEGENDplex (8 plex immunoglobulin isotyping panel, Biolegend) according to the manufacturer
429 procedure. Briefly, supernatants were incubated with analyte-specific antibody-coated microbeads for
430 1–2 hours. Supernatants were then washed and incubated with a PE-labeled secondary antibody for MFI
431 detection. Data were acquired on a LSRII (Becton-Dickinson) and Diva software and analyzed on
432 LEGENDplex data analysis software, comparing against standard curves for each analyte. Raw data were
433 normalized against tumor sample weights.

434

435 **Flow cytometry staining and acquisition**

436 Mononuclear cells were stained for live/dead Aqua, CD45-FITC, CD5-APC, CD19-PE-Cy7, CD20-PE-
437 Cf594, CD86- BV645, CD69-PE-Cy5.5, CD38-BV605, IgD-V450, CD27-BV785, CD21-BV711 and CD24-PE for
438 30 min at 4°C in PBS containing 2% FCS. Cells were then washed with PBS and fixed in 4% PFA for 20 min
439 at 4°C. After PBS washes, data were acquired on a LSRII (Becton-Dickinson). Marker expression was
440 compared against isotypic controls.

441

442 **Mass cytometry staining and acquisition**

443 Tumor cells were incubated with cisplatin (1 µM) to stain dead cells. Aspecific epitope binding was
444 blocked with 0.5 mg/mL human Fc Block (BD Biosciences, San Jose, CA, USA). Mononuclear cells were
445 stained for extracellular epitopes for 1h at 4°C, followed by permeabilization (FoxP3 permeabilization
446 reagent, eBioscience, San Diego, CA, USA) for 30 min at 4°C and intracellular marker staining with the
447 panels described in **Supplementary Tables S4–5**. Cells were then washed and labeled overnight with 125
448 nM iridium intercalator (Fluidigm, South San Francisco, CA, USA) in 2% PFA (Thermo-Fisher). Finally, cell
449 pellets were suspended in Milli-Q water (Merck Millipore, Burlington, MA, USA) containing 10% EQ four
450 element calibration beads (Fluidigm) and filtered through a 35 µm membrane before acquisition on a
451 mass cytometer (Helios® instrument, Fluidigm).

452

453 **Cytometry High-dimensional analysis**

454 *Flow cytometry analysis*

455 B cells were gated as $CD20^+$, $CD19^+$ or $CD20^+CD19^+$. h-SNE, which allows a better clustering of rare
456 populations such as tumor infiltrating cells (30 perplexity and 1,000 iterations, Cytosplore V2.2.1[63, 64]),
457 was then performed using CD5, IgD, CD38, CD86, CD21, CD27, and CD24 as clustering markers. Density
458 analysis was performed to identify and quantify B cell subpopulations. Clusters were secondarily
459 annotated according to marker expression.

460

461 *Mass cytometry analysis*

462 Myeloid cells ($CD45^+CD3^-CD19^-CD56^-CD33^+$) and T cells ($CD45^+CD3^+CD19^-CD33^-$) were manually
463 gated, then exported using FlowJo (Becton-Dickinson). Data were arcsinh-transformed with a cofactor of

464 5. Myeloid and T cell populations were automatically defined using h-SNE (using default settings of 30
465 perplexity and 1,000 iterations, Cytosplore V2.2.1)[63, 64], and density clustering was analyzed. For myeloid
466 cells, CD11b, CD1c, CD1a, CD11c, HLA-DR, CD123, CD303, CD141, CD163, CD206, PD-L1, CD40, IL-6, and
467 CD209 were used for clustering. For T cells, CD4, CD8, CD25, CD127, CTLA-4, PD-1, ICOS, CD69, CCR7,
468 CD45RA, and TIM3 were used for clustering.

469

470 **Between-group analysis (BGA)**

471 To assess the contribution of each variable to the discrimination of TLS^+ and TLS^- patient groups, a
472 BGA was performed, as previously described[65, 66]. Myeloid cells were identified by unsupervised
473 clustering, as described above. Variables with mean expression <5% and cell subsets with <30 cells were
474 excluded to avoid any assessment of background noises. BGA was performed using RStudio V1.3.1093, R-
475 4.0.3 (made4 package). R scripts performing BGA are provided in **Suppl. File S1**.

476

477 **Pagès Multiple factor analysis (MFA)**

478 To compare both clinical (FIGO, Age, LN, Emboli, Tumor size) and biological (DC count, B cell count,
479 DC density, B cell density, TLS) parameters we performed a Pagès Multiple factor analysis, which
480 determines the contribution of each parameter to the dimensions of a principal component analysis. In
481 our case it allowed to determine whether TLS and associated immune factors were associated to
482 negative parameters such as higher FIGO stage or lymphnode status or not. MFA allows the comparison
483 of both quantitative (DC count, B cell count, Age) and qualitative parameters (LN, TLS, DC density, B cell
484 density, FIGO, Tumor size, Emboli). MFA was performed using RStudio V1.3.1093, R-4.0.3. R scripts
485 performing BGA are provided in **Suppl. File S2**.

486

487 **Cell enrichment analysis**

488 CIBERSORT (Stanford University) was used for the immune cell enrichment analysis of the CESC
489 TCGA database. The individual gene expression file was uploaded to CIBERSORTx[67], and run using both
490 the relative and absolute modes, signature: LM22, 500 permutations, and disabled quantile
491 normalization (recommended for RNAseq data). For TLS scoring, enrichment scores for B cells, aDCs, and

492 $CD8^+$ T cells were scored as 1 (unenriched), 2 (poorly enriched), or 3 (highly enriched). Samples with high
493 enrichment in every cell subset were considered TLS^+.

494

495 **Statistical analysis**

496 TLS^- and TLS^+ tumors were discriminated by the morphology of T + B cell aggregates, their
497 presence *in situ*, and the quartile classification of B cell densities (1st quartile = 3.37 x 10^{-6} cells/µm²,
498 median = 3.31x10^{-5} cells/µm², 3rd quartile = 1.67.85 x 10^{-4} cells/µm²) and aDC densities (1st quartile =
499 70.19 x 10^{-6} cells/µm², median = 2.15x10^{-5} cells/µm², 3rd quartile = 4.85 x 10^{-5} cells/µm²). The 1st quartile
500 shows the lowest and the 4th quartile the highest densities. Aggregate presence and densities were then
501 scored according to the above-described parameters and tumors labeled as TLS^- and TLS^+.

502 Statistical analyses were generated using GraphPad Prism V8.00, with data expressed as mean ±
503 standard error of the mean. Statistical significance between two groups was calculated using the non-
504 parametric Mann–Whitney test, while multiple group comparisons were calculated using the non-
505 parametric Kruskal-Wallis test followed by a Dunn post-test. A p-value < 0.05 was considered as
506 significant. For survival analyses, PFS was defined as the time from diagnosis until death or relapse,
507 whichever occurred first. Patients without an event were censored at the time of their last follow up.
508 Survival times were estimated by the Kaplan–Meier method and compared using the log-rank test.

509

510 **Figure legends**

511 **Fig. 1: TLS in cervical tumors are associated with B cell density, dendritic cell activation and a higher**
512 **inflammatory profile. A**, Immunohistochemistry (IHC) staining for DC-LAMP, CD3, CD20 and CD21 in
513 n=34 cervical tumor samples. Tertiary lymphoid structures (TLS) were detected in 17/34 samples. **B**, B
514 cell density and mDC density in TLS-positive (TLS^+) and TLS-negative (TLS^-) cervical tumor samples. **C**, Bar
515 chart representing B cell and mDC numbers in TLS^- and TLS^+ tumors. **D**, Plot showing the correlation
516 between B cell and mDC numbers in n=34 cervical tumor samples. **E**, Images showing a representative
517 TLS, stained by multiplex IHC for CD20, CD3, DAPI, DC-LAMP, CD21 and PNAD. **F**, Soluble factors detected
518 in tumor supernatants by Luminex. The dot plot represents the concentration (pg/mL) of each protein in
519 healthy cervix, TLS^- and TLS^+ tumors. (*p<0.05, **p<0.01, *** p<0.005)

520 **Fig. 2: TLS-positive (TLS^+) tumors exhibit a higher B cell infiltrate characterized by an enrichment of**
521 **plasmablasts in the stromal compartment and exacerbated IgG presence. A**, Tumor-infiltrating B cells
522 characterized by flow cytometry. Data were analyzed by hierarchical stochastic neighborhood
523 embedding and density clustering. Clusters were annotated according to the expression of CD20, CD19,
524 CD21, CD27, IgD, CD24, CD86, and CD38. **B**, Number of gated B cells in TLS-negative (TLS^-) and TLS^+
525 tumors. **C**, Dot plot representing the B cell subpopulation within TLS^- and TLS^+ tumors. **D**, Multiplex
526 immunofluorescence for CD20, CD138, CD3, CD8, and PanCk on TLS^- (left, n=6) and TLS^+ (right, n=6)
527 tumor samples. Arrows in red squared regions highlight tumor nest B cells of interest. Arrows in yellow
528 squared regions highlight B cells of interest. **E**, Quantification of B cells ($CD20^+CD138^-$) , plasmablasts
529 ($CD138^+CD20^+$) and plasma cells ($CD138^+CD20^-PanCk^-$) in the tumor ($PanCk^+$) compartment. **F**,
530 Quantification of B cells ($CD20^+CD138^-$), plasmablasts ($CD138^+CD20^+$) and plasma cells ($CD138^+CD20^-$
531 $PanCk^-$) in the stromal ($PanCk^-$) compartment. **G**, Concentration of immunoglobulins in healthy cervix,
532 TLS^- and TLS^+ tumor supernatants. (*p<0.05, **p<0.01, *** p<0.005)

533

534 **Fig. 3: $CD163^+$ macrophages and activated cDC2 are enriched in TLS-positive (TLS^+) cervical tumors. A**,
535 Tumor-infiltrating myeloid cells analyzed by mass cytometry, h-SNE and density clustering. Clusters were
536 annotated according to the expression of markers in **Supplementary Table 5**. **B**, TAMs were gated and
537 quantified in n=14 samples and plotted according to the presence or absence of TLS. The plots show
538 higher frequency of $CD163^+$ TAM infiltrate in TLS^+ tumors. **C**, Multiplex immunohistochemistry (IHC)
539 results showing $CD163^+CD68^+$ and $CD163^-CD68^+$ TAMs in TLS^+ and TLS^- tumors. Representative images are
540 shown (top) and cell quantities were assessed (bottom). **D**, cDC2, $CD1a^{hi}$ LCs and $CD1a^{lo}$ DCs were gated
541 and quantified in n=14 samples and plotted according to the presence or absence of TLS. **E**, Multiplex IHC
542 results showing aDCs ($DC\text{-}LAMP^+CD1a^-$), aLCs ($DC\text{-}LAMP^+CD1a^+$) and iLCs ($DC\text{-}LAMP^-CD1a^+$) in TLS^+ and
543 TLS^- tumors. Representative images are shown (top) and cell quantities were assessed in the tumor nest
544 (center) and stroma (bottom). (*p<0.05)

545

546 **Fig. 4: Myeloid cells are more activated and better differentiated in TLS-positive (TLS^+) tumors. A**, The
547 flow chart represents myeloid population gating, marker extraction and filtering to assess each variable
548 contribution to TLS-negative (TLS^-) or TLS^+ tumors. **B**, Segregation biplot (left) showing the dispersion of
549 TLS^+ and TLS^- samples and the contribution of 44 variables to TLS^+ and 57 variables to TLS^-. The top 10
550 variables for TLS^+ and TLS^- tumors are represented on the waterfall plot. **C**, Plots showing quantified

551 frequencies of the top 10 variables from the TLS^+ group. (*p<0.05). **D**, Plots showing quantified
552 frequencies of the top 10 variables from the TLS^+ group. (*p-val<0.05).

553

554 **Fig. 5: Spatial analysis reveals increased interactions between aDCs and $CD8^+$ T cells, which exhibit**
555 **higher diversity in TLS-positive (TLS^+) tumors. A**, aDCs (DC-$LAMP^+CD1a^-$), a$CD1a^+$ DCs (DC-$LAMP^+CD1a^+$)
556 and i$CD1a^+$ DCs (DC-$LAMP^-CD1a^+$) identified by multiplex immunofluorescence (IF) in TLS^+ and TLS-
557 negative (TLS^-) tumors. **B**, Schematic representation of proximity analysis. **C**, Quantification of a$CD1a^{hi}$
558 proximity to $CD8^+$ T cells within 10 µm, 10–20 µm and 20–30 µm ranges in TLS^- and TLS^+ tumors. **D**,
559 Quantification of aDCs proximity to $CD8^+$ T cells within 10 µm, 10–20 µm and 20–30µm ranges in TLS^- and
560 TLS^+ tumors. **E**, Dot plots showing absolute counts of $CD8^+$ T cells subsets (naïve, EM, CM, TEMRA), which
561 were gated and quantified by mass cytometry. **F**, Dot plots showing absolute counts of $CD4^+$ T cells
562 subsets (naïve, EM, CM, TEMRA), which were gated and quantified by mass cytometry. **G**, $CD4^+$ T cell
563 analysis by hSNE and density clustering. The heatmap shows marker expression per cluster and each
564 cluster annotation. The violin plot shows the frequency of each cluster in TLS^+ and TLS^- samples. **F**, $CD8^+$ T
565 cell analysis by hSNE and density clustering. The heatmap shows marker expression per cluster and each
566 cluster annotation. The violin plot shows the frequency of each cluster in TLS^+ and TLS^- samples.
567 (*p<0.05).

568

569 **Fig. 6: TLS-positive (TLS^+) tumors with high B cell and DC densities are associated with improved**
570 **prognosis. A.** Plots of MFA in 32 patients highlighting TLS, B cell density and DC density as significant
571 discriminating factors. Left panel: MFA plot showing TLS^- (green) and TLS^+ (brown). Center panel: MFA
572 plot showing very low (green), low (brown), intermediate (blue) and high B cell density (pink). Right
573 panel: very low (green), low (brown), intermediate (blue) and high DC density (pink). **B,** Chart display of
574 the follow up of n=33 patients, annotated according to the absence of TLS (black, TLS^-), presence of TLS^+
575 B-DC $density^{hi}$ (red) or TLS^+B-DC $density^{lo}$ (blue). Crosses represent deaths and R represents relapses. **C,**
576 Kaplan-Meier plot showing progression-free survival (PFS) for patients in the 3 groups defined in **B**. **D**,
577 Immune cell enrichment algorithm Cibersort was used to investigate TIL infiltrate in TCGA CESC cohort
578 (309 patients). Kaplan-Meier curves were generated for scored TLS related cell types ($CD8^+$ Tcells, B cells
579 and activated DCs). A high score of enrichment for these cell types was labeled TLS^+ (green) and lower
580 scores were labeled TLS^- (black). *p<0.05.

581 **References**

582 1. Sung H, *et al.* Global Cancer Statistics 2020: GLOBOCAN Estimates of Incidence and Mortality
583 Worldwide for 36 Cancers in 185 Countries. *CA Cancer J Clin* **71**, 209-249 (2021).

584
585 2. Nayar R, Wilbur DC. The Pap test and Bethesda 2014. *Cancer Cytopathol* **123**, 271-281 (2015).

586
587 3. Odicino F, Pecorelli S, Zigliani L, Creasman WT. History of the FIGO cancer staging system. *Int J*
588 *Gynaecol Obstet* **101**, 205-210 (2008).

589
590 4. Tong WW, *et al.* Human papillomavirus 16-specific T-cell responses and spontaneous regression
591 of anal high-grade squamous intraepithelial lesions. *The Journal of infectious diseases* **211**, 405-
592 415 (2015).

593
594 5. Koskimaa HM, *et al.* Human papillomavirus 16 E2-, E6- and E7-specific T-cell responses in
595 children and their mothers who developed incident cervical intraepithelial neoplasia during a 14-
596 year follow-up of the Finnish Family HPV cohort. *J Transl Med* **12**, 44 (2014).

597
598 6. Woo YL, *et al.* A prospective study on the natural course of low-grade squamous intraepithelial
599 lesions and the presence of HPV16 E2-, E6- and E7-specific T-cell responses. *Int J Cancer* **126**,
600 133-141 (2010).

601
602 7. Cao L, Sun PL, He Y, Yao M, Gao H. Immune stromal features in cervical squamous cell carcinoma
603 are prognostic factors for distant metastasis: A retrospective study. *Pathol Res Pract* **216**, 152751
604 (2020).

605
606 8. Chen XJ, *et al.* Clinical Significance of CD163+ and CD68+ Tumor-associated Macrophages in
607 High-risk HPV-related Cervical Cancer. *J Cancer* **8**, 3868-3875 (2017).

608
609 9. Guo F, *et al.* The correlation between tumor-associated macrophage infiltration and progression
610 in cervical carcinoma. *Biosci Rep* **41**, (2021).

611
612 10. Kawachi A, Yoshida H, Kitano S, Ino Y, Kato T, Hiraoka N. Tumor-associated CD204(+) M2
613 macrophages are unfavorable prognostic indicators in uterine cervical adenocarcinoma. *Cancer*
614 *Sci* **109**, 863-870 (2018).

615
616 11. Colbert LE, *et al.* Expansion of Candidate HPV-Specific T Cells in the Tumor Microenvironment
617 during Chemoradiotherapy Is Prognostic in HPV16(+) Cancers. *Cancer Immunol Res* **10**, 259-271
618 (2022).

619

620 12. Li L, Ma Y, Liu S, Zhang J, Xu XY. Interleukin 10 promotes immune response by increasing the
621 survival of activated CD8(+) T cells in human papillomavirus 16-infected cervical cancer. *Tumour*
622 *Biol*, (2016).

623

624 13. Hanna BS*, et al.* Interleukin-10 receptor signaling promotes the maintenance of a PD-1(int) TCF-
625 1(+) CD8(+) T cell population that sustains anti-tumor immunity. *Immunity* **54**, 2825-2841 e2810
626 (2021).

627

628 14. Schumacher TN, Thommen DS. Tertiary lymphoid structures in cancer. *Science* **375**, eabf9419
629 (2022).

630

631 15. Fridman WH, Meylan M, Petitprez F, Sun CM, Italiano A, Sautes-Fridman C. B cells and tertiary
632 lymphoid structures as determinants of tumour immune contexture and clinical outcome. *Nat*
633 *Rev Clin Oncol* **19**, 441-457 (2022).

634

635 16. Dieu-Nosjean MC. Tumor-Associated Tertiary Lymphoid Structures: A Cancer Biomarker and a
636 Target for Next-generation Immunotherapy. *Adv Exp Med Biol* **1329**, 51-68 (2021).

637

638 17. Sautes-Fridman C*, et al.* Tertiary Lymphoid Structures in Cancers: Prognostic Value, Regulation,
639 and Manipulation for Therapeutic Intervention. *Front Immunol* **7**, 407 (2016).

640

641 18. Lin Z, Huang L, Li S, Gu J, Cui X, Zhou Y. Pan-cancer analysis of genomic properties and clinical
642 outcome associated with tumor tertiary lymphoid structure. *Sci Rep* **10**, 21530 (2020).

643

644 19. Ruffin AT*, et al.* B cell signatures and tertiary lymphoid structures contribute to outcome in head
645 and neck squamous cell carcinoma. *Nat Commun* **12**, 3349 (2021).

646

647 20. Horeweg N*, et al.* Tertiary lymphoid structures critical for prognosis in endometrial cancer
648 patients. *Nat Commun* **13**, 1373 (2022).

649

650 21. Guedj K*, et al.* M1 macrophages act as LTbetaR-independent lymphoid tissue inducer cells during
651 atherosclerosis-related lymphoid neogenesis. *Cardiovasc Res* **101**, 434-443 (2014).

652

653 22. Kang W*, et al.* Tertiary Lymphoid Structures in Cancer: The Double-Edged Sword Role in
654 Antitumor Immunity and Potential Therapeutic Induction Strategies. *Front Immunol* **12**, 689270
655 (2021).

656

657 23. Goc J*, et al.* Dendritic cells in tumor-associated tertiary lymphoid structures signal a Th1 cytotoxic
658 immune contexture and license the positive prognostic value of infiltrating CD8+ T cells. *Cancer*
659 *Res* **74**, 705-715 (2014).

660

661 24. de Chaisemartin L*, et al.* Characterization of chemokines and adhesion molecules associated with
662 T cell presence in tertiary lymphoid structures in human lung cancer. *Cancer Res* **71**, 6391-6399
663 (2011).

664

665 25. Liu Y, Cruikshank WW, O'Loughlin T, O'Reilly P, Center DM, Kornfeld H. Identification of a CD4
666 domain required for interleukin-16 binding and lymphocyte activation. *J Biol Chem* **274**, 23387-
667 23395 (1999).

668

669 26. Lynch EA, Heijens CA, Horst NF, Center DM, Cruikshank WW. Cutting edge: IL-16/CD4
670 preferentially induces Th1 cell migration: requirement of CCR5. *Journal of immunology* **171**,
671 4965-4968 (2003).

672

673 27. Kuo P, Tuong ZK, Teoh SM, Frazer IH, Mattarollo SR, Leggatt GR. HPV16E7-Induced Hyperplasia
674 Promotes CXCL9/10 Expression and Induces CXCR3(+) T-Cell Migration to Skin. *J Invest Dermatol*
675 **138**, 1348-1359 (2018).

676

677 28. Liang YK*, et al.* CXCL9 Is a Potential Biomarker of Immune Infiltration Associated With Favorable
678 Prognosis in ER-Negative Breast Cancer. *Front Oncol* **11**, 710286 (2021).

679

680 29. Li Z*, et al.* Epithelial mesenchymal transition induced by the CXCL9/CXCR3 axis through AKT
681 activation promotes invasion and metastasis in tongue squamous cell carcinoma. *Oncol Rep* **39**,
682 1356-1368 (2018).

683

684 30. Li M, He L, Zhu J, Zhang P, Liang S. Targeting tumor-associated macrophages for cancer
685 treatment. *Cell Biosci* **12**, 85 (2022).

686

687 31. Zhang XF*, et al.* The regulatory network of the chemokine CCL5 in colorectal cancer. *Ann Med* **55**,
688 2205168 (2023).

689

690 32. Aldinucci D, Borghese C, Casagrande N. The CCL5/CCR5 Axis in Cancer Progression. *Cancers*
691 *(Basel)* **12**, (2020).

692

693 33. Xu J*, et al.* Chordoma recruits and polarizes tumor-associated macrophages via secreting CCL5 to
694 promote malignant progression. *J Immunother Cancer* **11**, (2023).

695

696 34. Cambien B*, et al.* CCL5 neutralization restricts cancer growth and potentiates the targeting of
697 PDGFRbeta in colorectal carcinoma. *PloS one* **6**, e28842 (2011).

698

699 35. Dieu-Nosjean MC*, et al.* Long-term survival for patients with non-small-cell lung cancer with
700 intratumoral lymphoid structures. *J Clin Oncol* **26**, 4410-4417 (2008).

701

36. Karapetyan L, *et al.* Expression of lymphoid structure-associated cytokine/chemokine gene transcripts in tumor and protein in serum are prognostic of melanoma patient outcomes. *Front Immunol* **14**, 1171978 (2023).

37. Li C, Hua K. Dissecting the Single-Cell Transcriptome Network of Immune Environment Underlying Cervical Premalignant Lesion, Cervical Cancer and Metastatic Lymph Nodes. *Front Immunol* **13**, 897366 (2022).

38. Yao X, *et al.* Naturally acquired HPV antibodies against subsequent homotypic infection: A large-scale prospective cohort study. *Lancet Reg Health West Pac* **13**, 100196 (2021).

39. Beachler DC, Jenkins G, Safaeian M, Kreimer AR, Wentzensen N. Natural Acquired Immunity Against Subsequent Genital Human Papillomavirus Infection: A Systematic Review and Meta-analysis. *The Journal of infectious diseases* **213**, 1444-1454 (2016).

40. Safaeian M, *et al.* Risk of HPV-16/18 Infections and Associated Cervical Abnormalities in Women Seropositive for Naturally Acquired Antibodies: Pooled Analysis Based on Control Arms of Two Large Clinical Trials. *The Journal of infectious diseases* **218**, 84-94 (2018).

41. Gorvel L, Olive D. Tumor associated macrophage in HPV(+) tumors: Between immunosuppression and inflammation. *Semin Immunol* **65**, 101671 (2022).

42. Pittet MJ, Michielin O, Migliorini D. Clinical relevance of tumour-associated macrophages. *Nat Rev Clin Oncol* **19**, 402-421 (2022).

43. Park MD, Silvin A, Ginhoux F, Merad M. Macrophages in health and disease. *Cell* **185**, 4259-4279 (2022).

44. van Vlerken-Ysla L, Tyurina YY, Kagan VE, Gabrilovich DI. Functional states of myeloid cells in cancer. *Cancer Cell* **41**, 490-504 (2023).

45. Del Prete A, *et al.* Dendritic cell subsets in cancer immunity and tumor antigen sensing. *Cell Mol Immunol* **20**, 432-447 (2023).

46. Truxova I, *et al.* Mature dendritic cells correlate with favorable immune infiltrate and improved prognosis in ovarian carcinoma patients. *J Immunother Cancer* **6**, 139 (2018).

47. Minohara K, *et al.* Mature dendritic cells enriched in regulatory molecules may control regulatory T cells and the prognosis of head and neck cancer. *Cancer Sci* **114**, 1256-1269 (2023).

742 48. Duraiswamy J, *et al.* Myeloid antigen-presenting cell niches sustain antitumor T cells and license
743 PD-1 blockade via CD28 costimulation. *Cancer Cell* **39**, 1623-1642 e1620 (2021).

744
745 49. Haque A, *et al.* CD206(+) tumor-associated macrophages promote proliferation and invasion in
746 oral squamous cell carcinoma via EGF production. *Sci Rep* **9**, 14611 (2019).

747
748 50. Yagi T, *et al.* Tumour-associated macrophages are associated with poor prognosis and
749 programmed death ligand 1 expression in oesophageal cancer. *Eur J Cancer* **111**, 38-49 (2019).

750
751 51. Li Z, *et al.* The intratumoral distribution influences the prognostic impact of CD68- and CD204-
752 positive macrophages in non-small cell lung cancer. *Lung Cancer* **123**, 127-135 (2018).

753
754 52. Schweer D, McAtee A, Neupane K, Richards C, Ueland F, Kolesar J. Tumor-Associated
755 Macrophages and Ovarian Cancer: Implications for Therapy. *Cancers (Basel)* **14**, (2022).

756
757 53. Petitprez F, *et al.* B cells are associated with survival and immunotherapy response in sarcoma.
758 *Nature* **577**, 556-560 (2020).

759
760 54. Helmink BA, *et al.* B cells and tertiary lymphoid structures promote immunotherapy response.
761 *Nature* **577**, 549-555 (2020).

762
763 55. Zhang Y, *et al.* CD40 Accelerates the Antigen-Specific Stem-Like Memory CD8(+) T Cells
764 Formation and Human Papilloma Virus (HPV)-Positive Tumor Eradication. *Front Immunol* **11**,
765 1012 (2020).

766
767 56. Ceglia V, *et al.* Anti-CD40 Antibody Fused to CD40 Ligand Is a Superagonist Platform for Adjuvant
768 Intrinsic DC-Targeting Vaccines. *Front Immunol* **12**, 786144 (2021).

769
770 57. Vitale LA, *et al.* Development of CDX-1140, an agonist CD40 antibody for cancer immunotherapy.
771 *Cancer Immunol Immunother* **68**, 233-245 (2019).

772
773 58. Labiano S, *et al.* CD40 Agonist Targeted to Fibroblast Activation Protein alpha Synergizes with
774 Radiotherapy in Murine HPV-Positive Head and Neck Tumors. *Clin Cancer Res* **27**, 4054-4065
775 (2021).

776
777 59. Nywening TM, *et al.* Targeting tumour-associated macrophages with CCR2 inhibition in
778 combination with FOLFIRINOX in patients with borderline resectable and locally advanced
779 pancreatic cancer: a single-centre, open-label, dose-finding, non-randomised, phase 1b trial.
780 *Lancet Oncol* **17**, 651-662 (2016).

781

60. Dunbar KJ, *et al.* Tumor-Derived CCL5 Recruits Cancer-Associated Fibroblasts and Promotes Tumor Cell Proliferation in Esophageal Squamous Cell Carcinoma. *Mol Cancer Res* **21**, 741-752 (2023).

61. Zhai T, *et al.* Combination therapy with bevacizumab and a CCR2 inhibitor for human ovarian cancer: An in vivo validation study. *Cancer Med* **12**, 9697-9708 (2023).

62. Sautes-Fridman C, *et al.* Tertiary Lymphoid Structures and B cells: Clinical impact and therapeutic modulation in cancer. *Semin Immunol* **48**, 101406 (2020).

63. Ben Amara A, *et al.* High-throughput mass cytometry staining for deep phenotyping of human natural killer cells. *STAR Protoc* **3**, 101768 (2022).

64. van Unen V, *et al.* Visual analysis of mass cytometry data by hierarchical stochastic neighbour embedding reveals rare cell types. *Nat Commun* **8**, 1740 (2017).

65. Culhane AC, Perriere G, Considine EC, Cotter TG, Higgins DG. Between-group analysis of microarray data. *Bioinformatics* **18**, 1600-1608 (2002).

66. Fattori S, *et al.* Quantification of Immune Variables from Liquid Biopsy in Breast Cancer Patients Links Vdelta2(+) gammadelta T Cell Alterations with Lymph Node Invasion. *Cancers (Basel)* **13**, (2021).

67. Chen B, Khodadoust MS, Liu CL, Newman AM, Alizadeh AA. Profiling Tumor Infiltrating Immune Cells with CIBERSORT. *Methods Mol Biol* **1711**, 243-259 (2018).

Acknowledgements

We would like to thank the translational histopathology ICEP platform (CRCM, Marseille, France) for destocking patient FFPE blocks, and cutting the slides. We would like to thank the CRCM Cytometry platform (CRCM, Marseille, France) for their insights in panel design and access to cytometers. Editorial assistance for English language improvement was provided by Angloscribe, Calvisson, France.

Author contributions

L.G. and D.O. designed the project. L.G., J.S., C.D., and N.B., dissociated tumor samples. L.G., M.S.R., N.B., A.B.A., and J.S. performed the phenotyping experiment. L.G., N.B., and O.Q. performed the

817 soluble factor dosages and analysis. M.P. performed the IF staining and acquisitions. M.P. and L.G.
818 performed spatial analyses. L.G. analyzed CyTOF and flow cytometry experiments. X.C., R.S., E.L., and
819 O.Q. enrolled patients in the studies, performed patient follow-up, extracted clinical data and obtained
820 tumor samples. S.G. designed the BGA analysis, and L.G. and S.F. performed the analysis on cervical
821 tumors. L.G. and A.S.C. performed the statistical analyses and the MFA analysis of clinical data. L.G., M.P.
822 and M.C.D.N. interpreted the data. M.C.D.N. and D.O. supervised the project. L.G. drafted the
823 manuscript and designed the figures. All authors reviewed the manuscript and provided insights. We
824 declare that all authors contributed to the study and accept accountability of the data herein, and fulfil
825 the authorship criteria.

826

827 **Competing interests**

828 D.O. is a cofounder and shareholder of Imcheck Therapeutics, Alderaan Biotechnology, Emergence
829 Therapeutics, and Stealth IO, which did not take part in any part of the manuscript.

830 RS declares to have received research grants from Astra-Zeneca, consulting fees from GSK and EISAI, and
831 non-financial support from MSD, Astra-Zeneca, GSK, and Novartis, none of which participated to this
832 study.

833 EL declares to have received consulting fees from GSK and MSD, none of which participated to this study.

834 Other authors declare no conflict of interest.

835

836 **Additional information**

837 **Correspondence** and requests for materials should be addressed to Laurent Gorvel
838 (laurent.gorvel@inserm.fr) or Daniel Olive (daniel.olive@inserm.fr).

839

Table 1: Clinical characteristics of cervical cancer patients

		Tumor samples*	Healthy samples
Characteristic	**-**	**n=34**	**n=5**
Age, median (range)	*Current (years)*	58 (37-80)	
	At diagnosis (years)	53 (32-77)	
Histology, n	*SCC***	24	*NA*
	*ADK***	5	*NA*
	*Other***	*1*	*NA*
FIGO stages, n	*IB1*	4	*NA*
	IIA1	2	*NA*
	IIA2	1	*NA*
	IIB	14	*NA*
	IIIA	1	*NA*
	IIIB	3	*NA*
	IIIC1	5	*NA*
	IVA	2	*NA*
	IVB	2	*NA*
Emboli, n	*Positive*	3	0
	Negative	31	5
LN invasion, n	*Positive*	14	0
	Negative	20	5
Adverse events, n	**Metastasis**	4	0
	Relapses	5	0
	Deaths	2	0

**Note: cervical tumors are considered 100% HPV+*
*** Note: SCC: squamous cell carcinoma; ADK: adenocarcinoma; Other: mixed origins, serous, clear cell carcinomas*

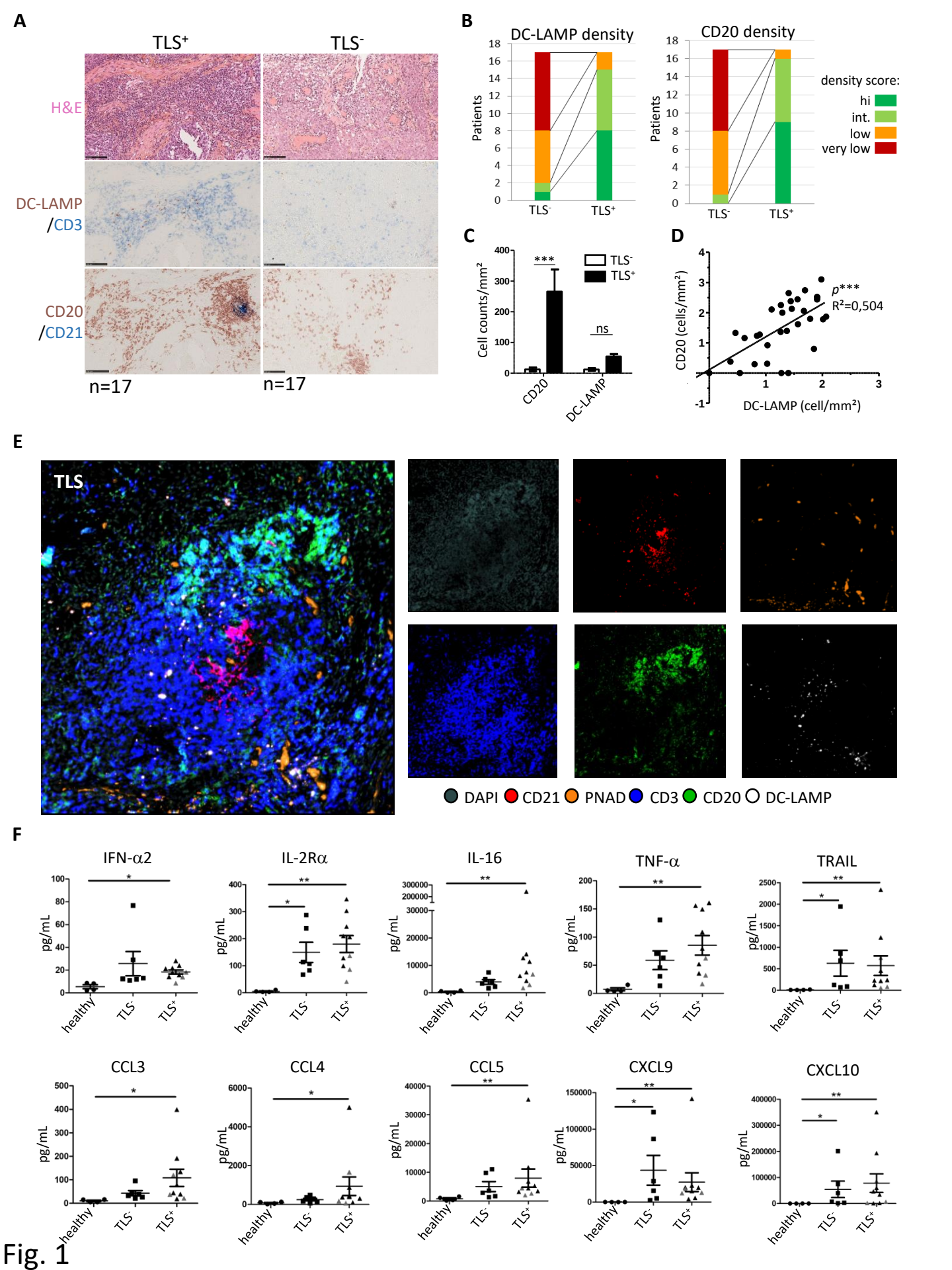
A
TLS+
TLS-
H&E
DC-LAMP /CD3
CD20 /CD21
n=17
n=17
B
DC-LAMP density
CD20 density
Patients
TLS-
TLS+
density score:
hi
int.
low
very low
C
Cell counts/mm²
***
ns
TLS-
TLS+
CD20
DC-LAMP
D
CD20 (cells/mm²)
DC-LAMP (cell/mm²)
p***
R²=0,504
E
TLS
DAPI
CD21
PNAD
CD3
CD20
DC-LAMP
F
IFN-α2
IL-2Rα
IL-16
TNF-α
TRAIL
CCL3
CCL4
CCL5
CXCL9
CXCL10
pg/mL
healthy
TLS-
TLS+

Fig. 1

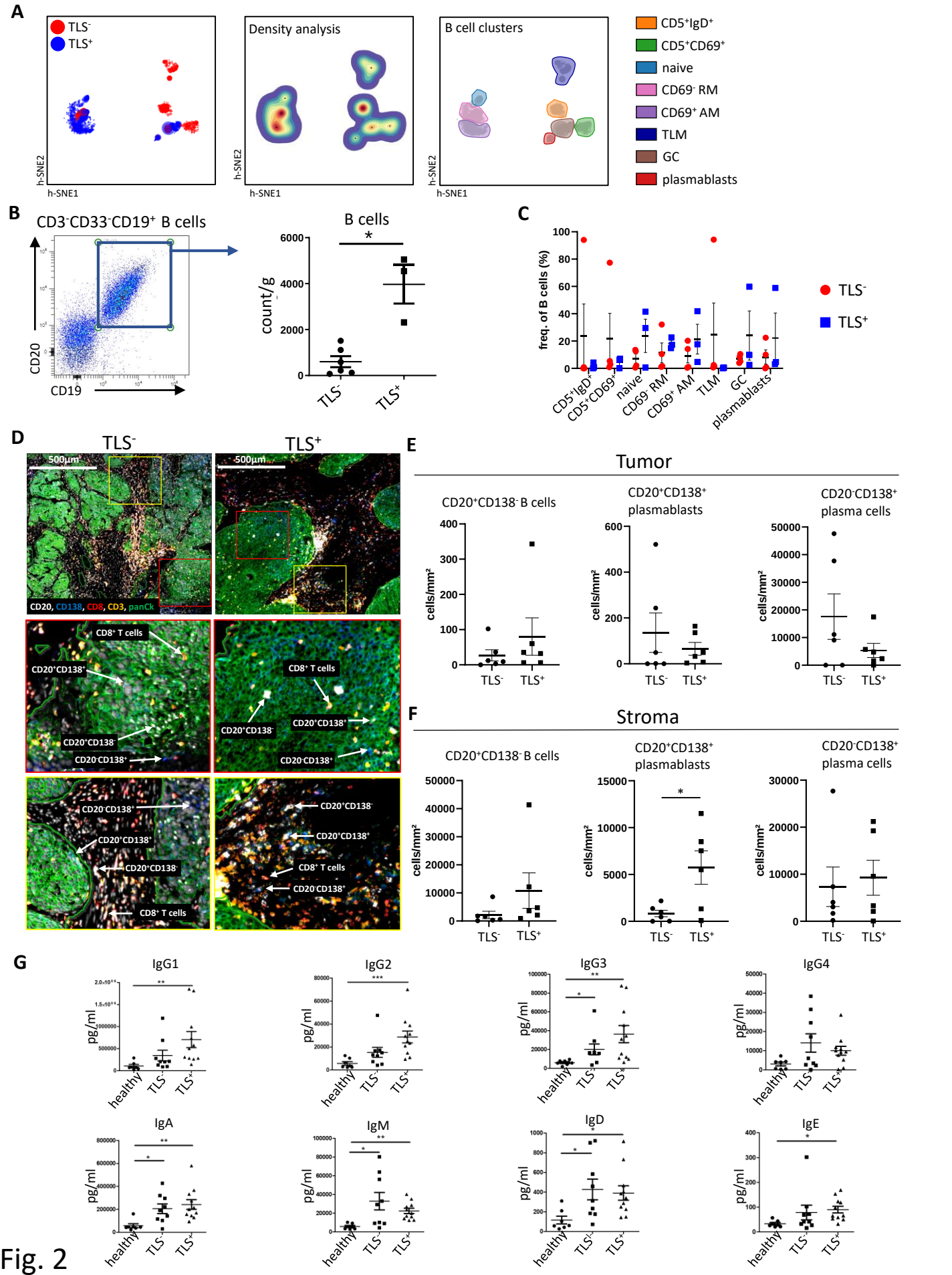
A
TLS⁻
TLS⁺
h-SNE2
h-SNE1
Density analysis
B cell clusters
CD5⁺IgD⁺
CD5⁺CD69⁺
naive
CD69⁻ RM
CD69⁺ AM
TLM
GC
plasmablasts
B
CD3⁻CD33⁻CD19⁺ B cells
CD20
CD19
B cells
count/g
TLS⁻
TLS⁺
C
freq. of B cells (%)
D
TLS⁻
TLS⁺
500µm
CD20, CD138, CD8, CD3, panCk
CD8⁺ T cells
CD20⁺CD138⁺
CD20⁺CD138⁻
CD20⁻CD138⁺
E
Tumor
CD20⁺CD138⁻ B cells
CD20⁺CD138⁺ plasmablasts
CD20⁻CD138⁺ plasma cells
cells/mm²
F
Stroma
G
IgG1
IgG2
IgG3
IgG4
IgA
IgM
IgD
IgE
pg/ml
healthy

Fig. 2

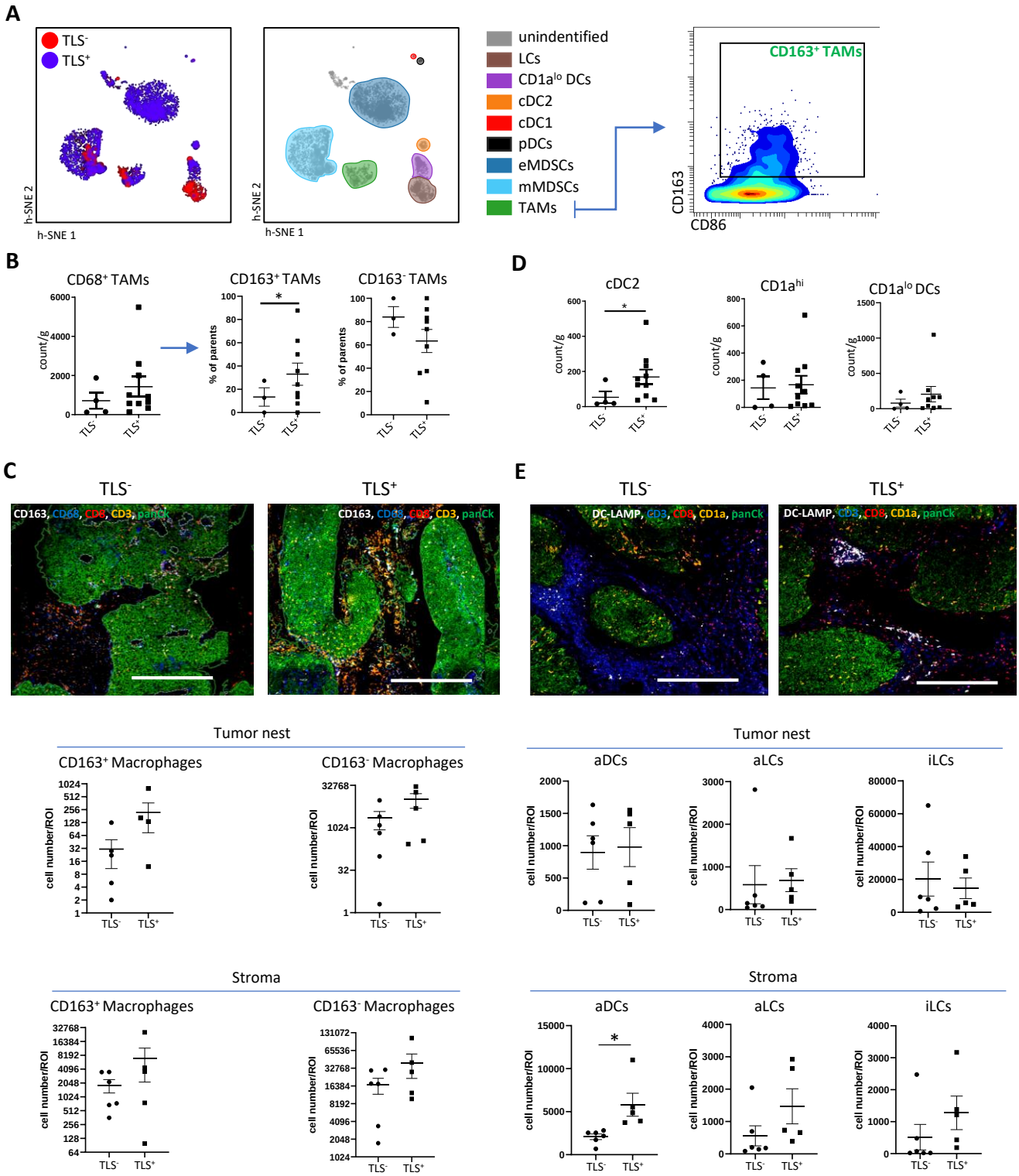
A
TLS-
TLS+
h-SNE 2
h-SNE 1
unindentified
LCs
CD1a^lo DCs
cDC2
cDC1
pDCs
eMDSCs
mMDSCs
TAMs
CD163+ TAMs
CD163
CD86
B
CD68+ TAMs
CD163+ TAMs
CD163- TAMs
count/g
% of parents
D
cDC2
CD1a^hi
CD1a^lo DCs
C
TLS-
TLS+
CD163, CD68, CD8, CD3, panCK
E
DC-LAMP, CD3, CD8, CD1a, panCK
Tumor nest
CD163+ Macrophages
CD163- Macrophages
aDCs
aLCs
iLCs
cell number/ROI
Stroma

Fig. 3

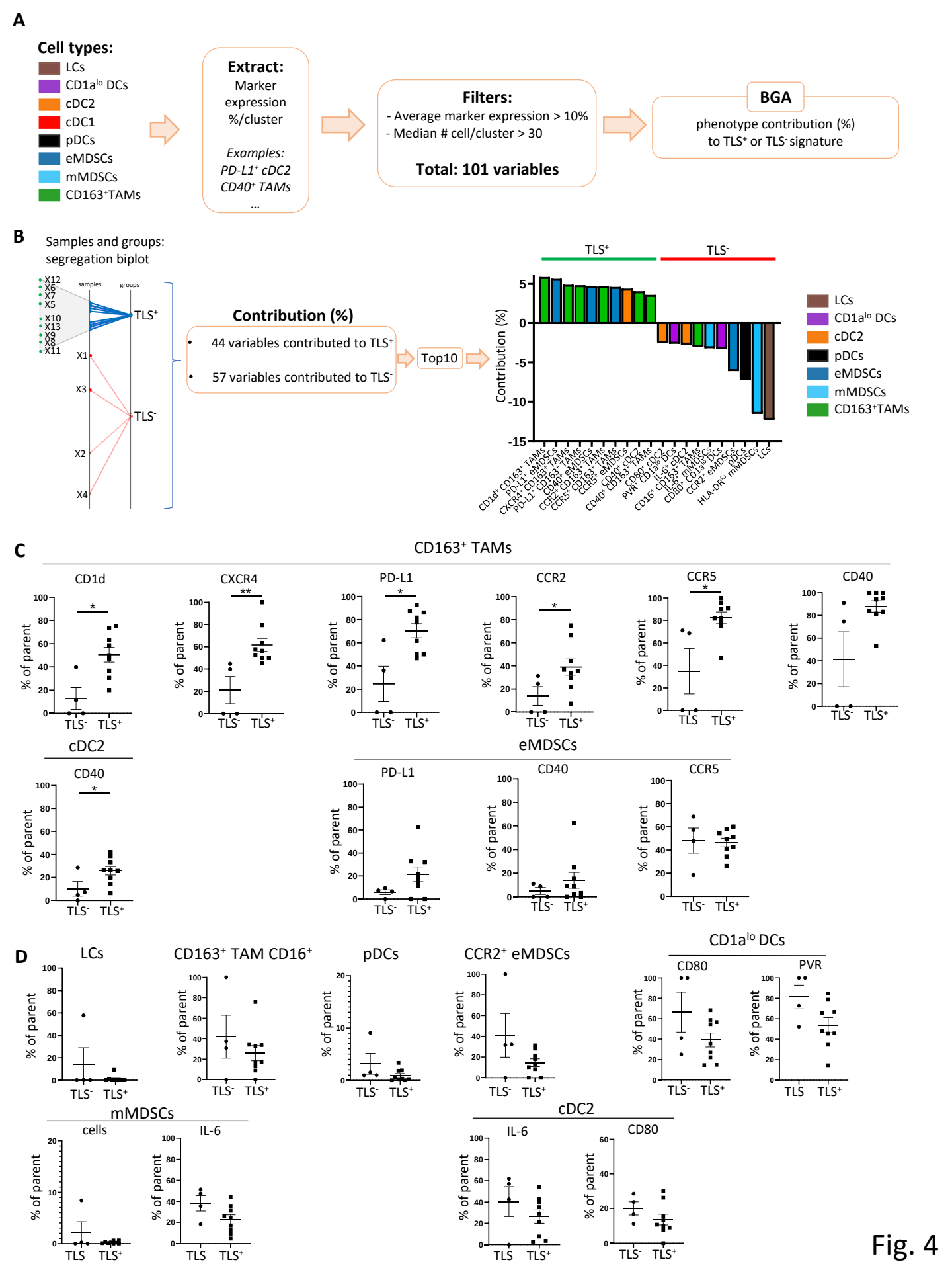
A
Cell types:
LCs
CD1a^lo DCs
cDC2
cDC1
pDCs
eMDSCs
mMDSCs
CD163⁺TAMs
Extract:
Marker expression %/cluster
Examples:
PD-L1⁺ cDC2
CD40⁺ TAMs
...
Filters:
- Average marker expression > 10%
- Median # cell/cluster > 30
Total: 101 variables
BGA
phenotype contribution (%) to TLS⁺ or TLS⁻ signature
B
Samples and groups: segregation biplot
samples
groups
TLS⁺
TLS⁻
Contribution (%)
44 variables contributed to TLS⁺
57 variables contributed to TLS⁻
Top10
Contribution (%)
C
CD163⁺ TAMs
CD1d
CXCR4
PD-L1
CCR2
CCR5
CD40
% of parent
TLS⁻
TLS⁺
cDC2
CD40
eMDSCs
PD-L1
CD40
CCR5
D
LCs
CD163⁺ TAM CD16⁺
pDCs
CCR2⁺ eMDSCs
CD1a^lo DCs
CD80
PVR
mMDSCs
cells
IL-6
cDC2
IL-6
CD80

Fig. 4

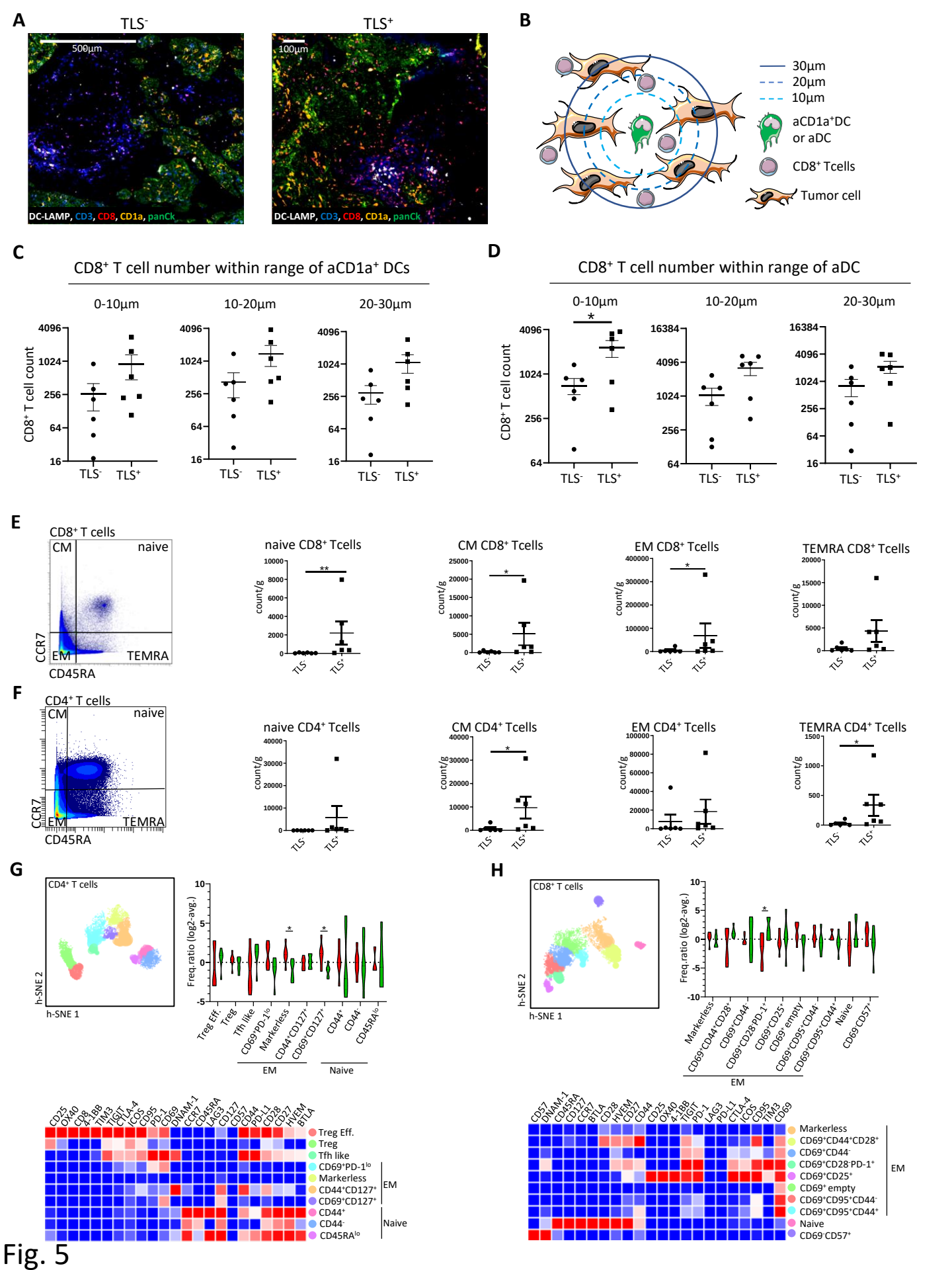
A
TLS-
TLS+
500µm
100µm
DC-LAMP, CD3, CD8, CD1a, panCk
B
30µm
20µm
10µm
aCD1a+DC or aDC
CD8+ Tcells
Tumor cell
C
CD8+ T cell number within range of aCD1a+ DCs
0-10µm
10-20µm
20-30µm
CD8+ T cell count
TLS-
TLS+
D
CD8+ T cell number within range of aDC
E
CD8+ T cells
CM
naive
EM
TEMRA
CCR7
CD45RA
naive CD8+ Tcells
CM CD8+ Tcells
EM CD8+ Tcells
TEMRA CD8+ Tcells
count/g
F
CD4+ T cells
naive CD4+ Tcells
CM CD4+ Tcells
EM CD4+ Tcells
TEMRA CD4+ Tcells
G
CD4+ T cells
h-SNE 1
h-SNE 2
Freq.ratio (log2-avg.)
Treg Eff.
Treg
Tfh like
CD69+PD-1lo
Markerless
CD44+CD127+
CD69+CD127+
CD44+
CD44-
CD45RAlo
EM
Naive
H
CD8+ T cells
Markerless
CD69+CD44+CD28+
CD69+CD44-
CD69+CD28-PD-1+
CD69+CD25+
CD69+ empty
CD69+CD95+CD44-
CD69+CD95+CD44+
Naive
CD69+CD57+

Fig. 5

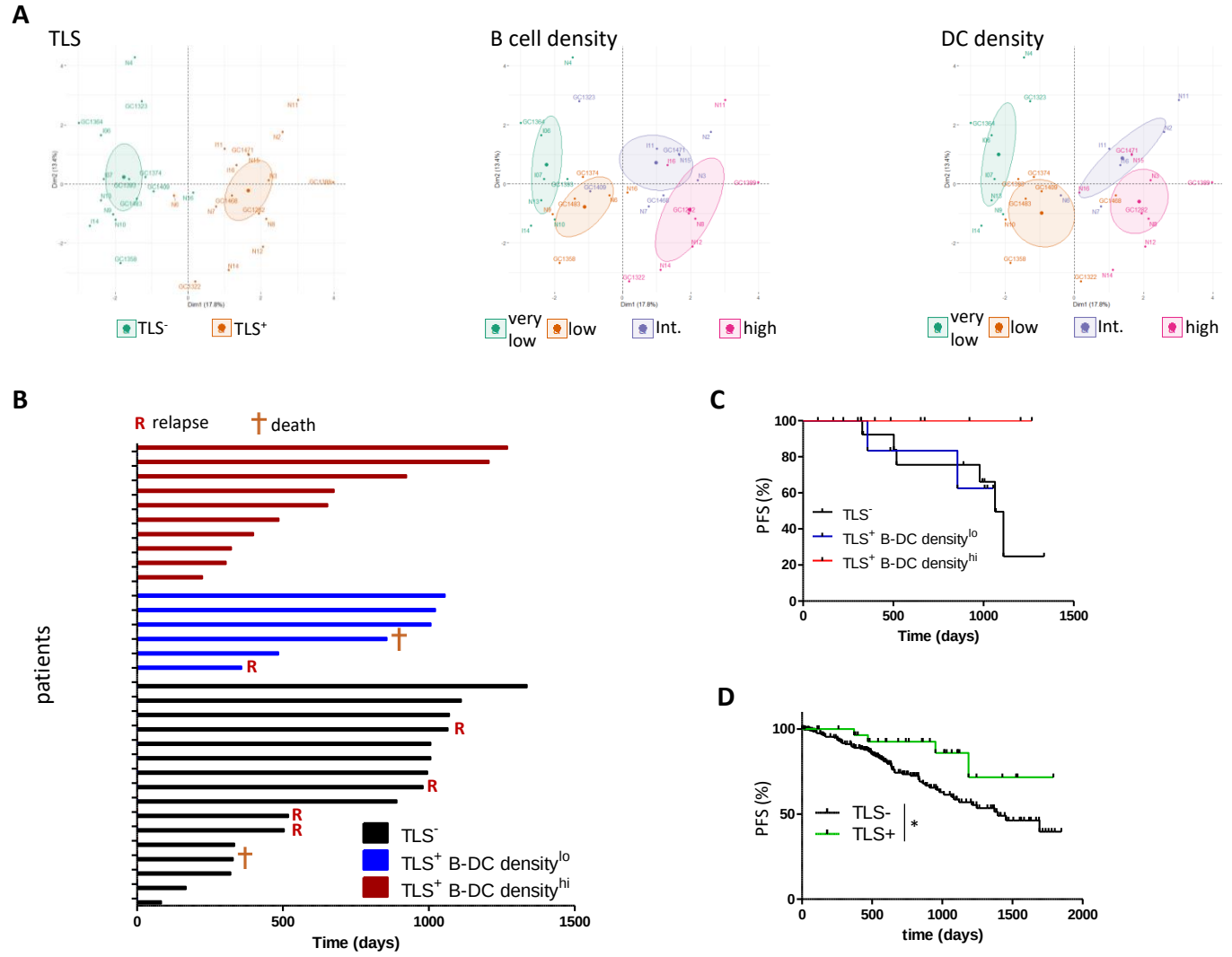
A
TLS
B cell density
DC density
TLS-
TLS+
very low
low
Int.
high
B
R relapse
† death
patients
TLS-
TLS+ B-DC density lo
TLS+ B-DC density hi
Time (days)
C
PFS (%)
TLS-
TLS+ B-DC density lo
TLS+ B-DC density hi
Time (days)
D
PFS (%)
TLS-
TLS+
*
time (days)

Fig. 6